Assembly of Nanorods into Designer Superstructures: The Role of Templating, Capillary Forces, Adhesion, and Polymer Hydration

Jacob. W. Ciszek,[†,‡,*] Ling Huang,[†,¶] Stefan Tsonchev,[†,§] YuHuang Wang,[†,#] Kenneth R. Shull,[⊥,*] Mark A. Ratner,[†,*] George C. Schatz,[†,*] and Chad A. Mirkin[†]

[†]Department of Chemistry and International Institute of Nanotechnology, Northwestern University, Evanston, Illinois 60208, [§]Department of Chemistry, Northeastern Illinois University, Chicago, Illinois 60625, and [⊥]Department of Materials Science and Engineering, Northwestern University, Evanston, Illinois 60208. [¶]Current address: School of Chemical and Biomedical Engineering, Nanyang Technological University, Singapore 637457. [#]Current address: Department of Chemistry and Biochemistry, University of Maryland, College Park, Maryland 20742. [‡]Current address: Department of Chemistry, Loyola University, Chicago, Illinois 60626.

ABSTRACT The assembly mechanism by which hundreds of thousands of two-segment gold-polypyrrole nanorods are assembled into kinetically controlled shape-directed superstructures is examined to predict the range of nanoparticle sizes and materials that can be utilized in their formation. Four processes are responsible for assembly: templating, capillary force assembly, adhesion, and polymer hydration. It is shown that templating, where rods are prepositioned for assembly, is scale invariant and that the energy-minimized state after this step is highly disordered. In addition, we predict that superstructures can be made independently from patterns of rods separated by a distance as small as six times the inter-rod spacing. Both modeling and experiment show that adhesion and polymer dehydration, which induces curvature in the superstructures, are applicable to other materials. However, the high surface energy and low elastic modulus of polypyrrole are advantageous toward generating three-dimensional structures, inducing curvature at gold/polypyrrole length ratios as large as 7:1.

KEYWORDS: nanorods · self-assembly · templating · adhesion · capillary force assembly

A general goal of nanoscience is to learn how to assemble nanoscale building blocks into preconceived higher order architectures with properties that are derived from the type and placement of such building blocks within the extended material. When the building blocks are nanoparticles rather than discrete molecules, assembly strategies are limited. Thus far, methods based upon hydrophobic,[1] electrostatic,[2] magnetic,[3] DNA hybridization,[4,5] and capillary forces[6] have been evaluated and used to prepare impressive structures such as rings, pyramids, and network materials with varying degrees of success. Recently, we introduced the concept of kinetically controlled, template-directed assembly, where rod-shaped nanoparticles could be assembled into discrete superstructures that could be deliberately varied in shape, depending upon the type of template used, and the composition, length, and diameter of the rods.[7] Importantly, in this work, one set (but different numbers) of nanorods could be directed to assemble into different high-order architectures (globes, hemispheres, and open spheres). Upon detailed examination of this system, we have discovered that a complex combination of micro/nanoscale phenomena and experimental variables are responsible for the assembly process—specifically, templating, capillary force assembly, adhesion, and polymer dehydration. Herein, we explore the roles and relative importance of each of these factors in governing the assembly of the rods into the intended higher order architectures. Moreover, we develop a set of general guidelines for using these factors to reliably synthesize superstructures from templated sets of nanoparticle building blocks.

RESULTS AND DISCUSSION

Superstructure Assembly. The assembly process begins with two-part gold-polypyrrole (Ppy) nanorods synthesized inside an anodic aluminum oxide (AAO) template *via* the method pioneered by Martin and by Moskovits.[8,9] Briefly, a silver backing is evaporated onto the template (Whatman, Figure 1a) which serves as a working electrode for electrochemically depositing the Au and Ppy into the pores. Upon dissolution of the AAO template, Au−Ppy rods, which on average have a 185 ± 14 nm radius (*r*) and a length between 5 and 30 (±~15%) μm (*l*), assemble into curved superstructures, with

*Address correspondence to jciszek@luc.edu, ratner@chem.northwestern.edu, k-shull@northwestern.edu, schatz@chem.northwestern.edu.

Received for review October 8, 2009 and accepted December 14, 2009.

Published online December 30, 2009. 10.1021/nn901383d

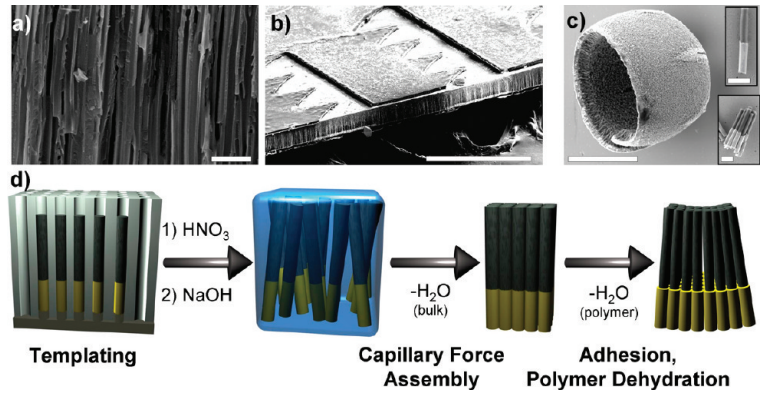

Figure 1. Superstructure shape control. (a) An SEM image of the pores of a bare AAO membrane used as a template for nanorod generation. (b) The AAO template is patterned with photoresist (darker elevated pattern). The areas covered by photoresist are not exposed to the plating/polymerization solution and rods are electrochemically deposited exclusively in the uncovered areas (rods are the light areas at the bottom of the template). (c) After the template is removed the rods assemble into a superstructure (in this case a hemisphere) whose shape is determined by the photoresist pattern in conjunction with the template. The insets show typical two-part Au−Ppy rods which comprise the curved superstructures. (d) A scheme showing each step of the assembly process and a description of the manipulations responsible for generating the kinetically controlled superstructures. After dissolving the template holding the rods, a loose collection of rods remains in water (blue). The bulk water evaporates, and the rods are brought together. When the water contained within the Ppy evaporates, the Ppy segment shrinks, which induces curvature. Scale bars in panels a, b, and c are 2, 300, and 100 μm, respectively. Inset scale bars are 1 μm. In panel d, the inter-rod spacing has been exaggerated for visual clarity.

the radius of curvature of the final structure dictated by the gold and polypyrrole segment lengths.[10,11] To effect shape control over the superstructures, a pattern of photoresist can be used to block pores of the template selectively, preventing electrodeposition in undesired regions (Figure 1b). This templates, or prepositions the rods, such that when the AAO is dissolved and the rods are released, they assemble into superstructures consisting of hundreds of thousands of rods ($5.3 \pm 0.5 \times 10^5$ for a hemisphere pattern, $1.6 \pm 0.1 \times 10^6$ for a cross pattern) with the template providing shape-control (Figure 1c). The rod assembly occurs in three distinct steps (Figure 1d). In step one, the template is dissolved but little discernible rod movement is observed. The nanorods are spaced an average of 32 ± 9 nm apart both in the template and in solution (as confirmed by SEM and optical microscopy)[7] and their separation does not change over time so long as the collection of rods remains surrounded by water. In step two, the water between the rods evaporates, the rods are brought together *via* capillary forces, and a more densely packed structure is observed. In the final step, additional water evaporation occurs, the polypyrrole segments of the rods dehydrate, their diameters shrink, resulting in a pseudoconical building block, and curvature is induced in the superstructure of rods. Each of these steps is essential to the formation of the observed superstructures. Some of them can be deliberately manipulated to control the dimensions of the final superstructure.

Prepositioning of Rods. The first and most important step is the prepositioning of rods *via* the alumina template. Templating provides three functions: constraining rod orientation *via* the pores, determining rod placement in the template *via* the photoresist pattern, and controlling inter-rod spacing *via* the spacing of the pores. Since the nature of the template prevents varying the rod orientation, we examined the importance of rod spacing and rod placement by varying the template. The former was studied by Monte Carlo simulations, and the latter was studied by a combination of theory and experimental laboratory procedures.

In our analysis, when a rod is defined as part of a particular pattern it is assumed that the rod does not dissociate and assemble into an adjacent pattern. This assumption is supported by the shape control reported previously—if dissociation occurred one would expect a thermodynamic product with no shape control provided by the pattern. However, as the spacing between these two patterns (*x* in Figure 2a) decreases, the distance between patterns eventually approaches the spacing between rods inside the pattern. At this point random motion will cause a portion of the rods to transfer from one pattern to the next and the pattern's shape will be distorted. To examine the limits of rod placement and patterning for generating kinetically controlled structures we focused on reducing the interpattern spacing *x*. In our original paper, patterns in the template were separated by 400 and 200 μm.[7] We reduced this spacing using square patterns separated by 100 and 50 μm (Figure 2a). At all pattern spacings, the assemblies retain their original shape and there is no evidence of rod exchange, as determined by optical microscopy and SEM. However, the smaller spacings are really of interest. Below a pattern spacing of 5 μm[12] it becomes challenging to use photolithography to pattern the alumina template which is 50% porous (factory specifications, Supporting Information, Figure S1). To

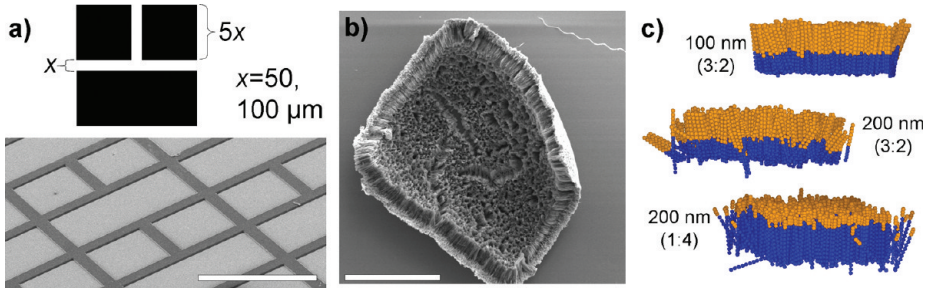

Figure 2. (a) Top: lithography pattern for generating specific spacing (*x*) between superstructures. Bottom: an SEM of the corresponding photoresist pattern (dark areas) on an AAO template. Lighter areas are exposed pores. (b) SEM image of a 250 μm square superstructure after curving. (c) Images of converged systems generated from Monte Carlo simulations where the spacing in-between rods is varied. From the top: 3:2 Au:Ppy rods with 100 nm initial spacing; 3:2 Au:Ppy rods with 200 nm initial spacing; 1:4 Au:Ppy rods with 200 nm initial spacing. Scale bars in panels a and b are 1 mm and 100 μm, respectively.

examine pattern spacings below this size regime, we performed Monte Carlo simulations on a similar collection of rods, without a template.

The simulations were performed by modeling the rods as connected spheres[13] ("string of pearls" structure) with a diameter equal to the corresponding dimension of the nanorod segment. Rods are 4.5 μm long with a gold to polypyrrole segment-length ratio of 3:2 or 1:4. The number of spheres per segment is determined by the length of the segment divided by the sphere diameter which is then rounded up to the nearest integer. In a typical simulation, the initial state of the system is a square pattern made of 100 or 400 rods (10 × 10 or 20 × 20). The two primary forces between the segments are metal−metal (M−M) and hydrophobic (hy) interactions with the interaction energies per unit area between the rods' component spheres modeled by the formulas

$$E_{M-M} = -2\gamma_{SL,Au}(1 + L/\lambda_{Au})\, e^{-L/\lambda_{Au}} \quad (1)$$

and

$$E_{hy} = -2\gamma_{SL,Ppy}\, e^{-L/\lambda_{Ppy}} \quad (2)$$

respectively.[14] Here the γ_{SL} are the surface tensions of Au and Ppy in water (1.54 and 0.33 J/m^2),[15,16] λ_{Au} is the Thomas−Fermi screening length for Au (0.588 Å),[17] λ_{Ppy} is the characteristic decay length of the hydrophobic interaction for Ppy (2 nm),[14] and L is the distance between the component spheres. The weaker van der Waals interactions between the gold and the polypyrrole segments are ignored in the simulations. The potential energy landscape of the system is sampled by jumps on the order of 10^8 kT at room temperature, which is of the same order of magnitude as the interaction energy of two such rods in contact, and simulations were run until the energy of the system converged. In the simulations the rods are allowed to translate and rotate in three dimensions. Both single rods and clusters of rods are allowed to move according to the data augmentation algorithm.[18]

To examine the effect of the pattern spacing (*x*) between initial squares of aligned rods on the ability to maintain the predefined pattern shape, we varied the spacing between two 10 × 10 patterns starting from 64 nm (or twice the inter-rod distance) to 192 nm, and examined the probability for rod exchange between the squares in the final state. The data are reported as a percentage of the rods of the two faces closest to each other (20 rods) that are exchanged between squares. We observe that in the case when $x = 64$ nm there is a significant rod exchange between the two interfaces (20%). When the spacing is increased this percentage remains about the same, up to a spacing of 160 nm. Then, at a spacing of 192 nm, the number is zero for any reasonable time scale. Thus, we can predict that the ultimate limit for the assembly process would be 192 nm, or a pattern spacing of six times the inter-rod distance. This behavior is dependent on both the rod length and spacing, as well as pattern spacing, and we expect that systems with dimensions of similar ratios would behave similarly (discussed below).

In addition to controlling the number of rods that can participate in an assembly process, the template also controls the spacing between the rods. To examine the role of inter-rod spacing within a single square pattern on the assembly process, we simulated systems with rod spacings significantly larger than the experimental distance (32 ± 9 nm). Spacings of 100, 200 (Figure 2c), and 300 nm, respectively, were studied. In these simulations, for inter-rod distances up to 200 nm, the intended shape (a square raft) is maintained. However, with a spacing of 300 nm the rods disperse, and the intended structure does not form. This is *not* based on the decay of the hydrophobic force[19] over distance. Indeed, as follows from eq 2, the hydrophobic force is negligible at *both* 200 and 300 nm inter-rod spacings. Moreover, even if the interactions are strengthened (by doubling the length of the polypyrrole section, giving stronger hydrophobic forces) no difference in the final superstructure is seen. Shape control, instead, is dominated by the random motion (entropy) of the rods and

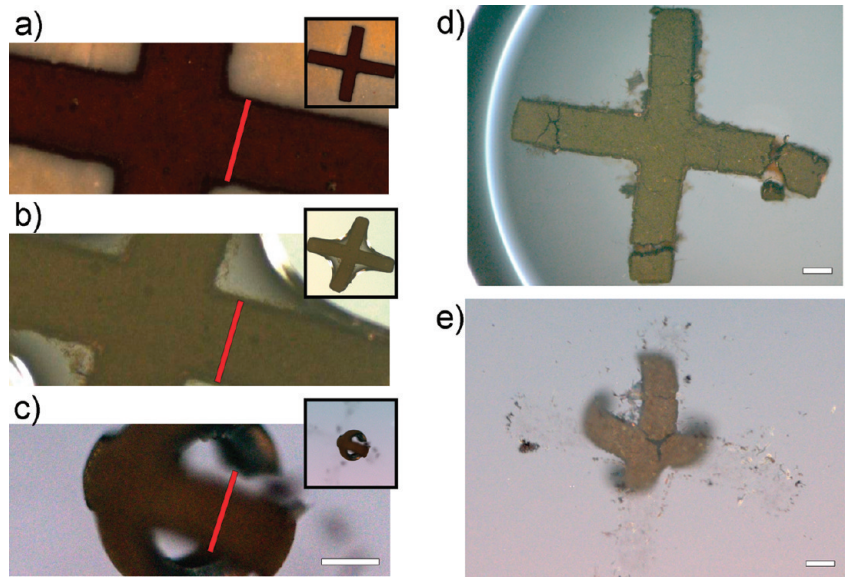

Figure 3. Optical images of a cross-shaped grouping of rods: (a) Rods immobilized in an anodic aluminum oxide template; (b) the grouping of rods where the template has been dissolved; (c) bulk water has been removed from the system, capillary forces have drawn the rods together, and the structure's dimensions have been reduced. Images a through c are the same scale and the 80% reduction in the object size can be seen in image c. The red bar in image c is the original arm dimension (seen in images a and b). (d) A superstructure that has been damaged during handling. Note that in both the right and lower arms, fractures have broken the structure into sections separated by ~40 μm. (e) After capillary force assembly and adhesion mediated curving, these sections have been assembled into the main structure. Scale bars are 100 μm. Insets are 15% of the size of the original.

the *dimensions* of the system (in addition to templating). At 200 nm random motion both translates and rotates the rods. A small percentage of movements (or more accurately, a sequence of movements) will rotate the top (or bottom) of a rod toward its nearest neighbor (within the square), or translate a rod into contact with its neighbor. At this point the hydrophobic and metal−metal interactions become significantly larger and restrict the motion of the rods. This must happen before the random movements (entropy) cause the rods to escape from the edge of the pattern (or from the plane of the initial matrix). When the spacing is increased to 300 nm, a sequence of movements leading to connections between rods becomes statistically less likely, and entropy dominates, dispersing the rods.

There are two additional noteworthy points about the Monte Carlo simulations. First, the templating is scale invariant for a wide range of sizes. Since inter-rod forces are insignificant until near contact, and random rod movement dominates, a pattern of rods where l = 4.5 μm, r = 200 nm, and the distance between rods is 200 nm, will behave almost identically to a pattern where l = 9 μm, r = 400 nm, and the distance between rods is 400 nm, since they are identical from the perspective of the random rod movement. We expect that for very large rods, gravity would lead to deviation from scale invariant behavior. Second, the converged system contains a large degree of small angle orientational disorder, where rods are randomly connected in a nonparallel, noncoalesced fashion (second image in Figure 1d). This network of disordered interconnected rods stabilizes the dimension of the system in solution and leads to the retention of its initial size until an additional force is applied. This agrees with experimental results (Figure 3a,b) which show that the superstructure dimensions do not change while in solution.

Capillary Force Assembly. While hydrophobic and metal−metal forces are sufficient to sustain the loose collections of rods in solution, they are insufficient to assemble the rods into cofacial contact. Thus, a second, stronger, force[20] must be applied to bring the network of rods together—in this case capillary forces.[21] These forces have been empirically studied and have been shown to be significant over a distance of several micrometers and sufficiently strong to bring together nanoparticles into network solids.[22,23] Indeed, capillary forces are the basis of the standard methods for preparing such network structures.[24] More quantitatively, they have been shown to be 2 orders of magnitude larger than hydrophobic forces at particle spacings similar to ours (albeit with different particle sizes and geometry).[20,25] Precise numerical solutions for parallel rod systems are possible for large inter-rod spacings relative to the rod radius; however, they become nontrivial as the ratio of those distances decreases and the contact angle between the water and the rod's surface becomes a function of the inter-rod distance. Theory describing the difficulties in the quantitative treatment of the capillary forces (along with numerical solutions for highly simplified systems) is provided elsewhere.[6,26,27]

The role of capillary forces can be observed by optical microscopy (Figure 3). For a cross-like structure, the initial photoresist pattern has an "arm" width of 143 ± 1

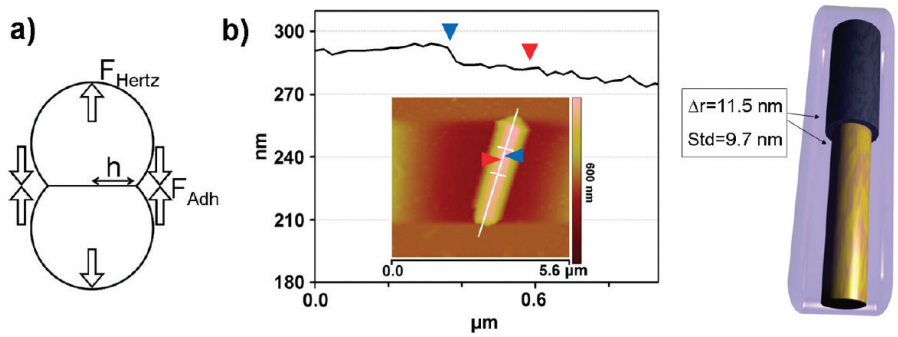

Figure 4. (a) Illustration of the two major forces involved in adhesion. The adhesive force brings the two flattened cylinders together while the Hertzian (restoration from deformation) force opposes it. (b) AFM data of a typical rod and an illustration highlighting statistical information. AFM data show both the image of the rod (inset) as well as height data. Height data are taken from along the line in the image. The Ppy segment is on the left side of the profile and the arrows highlight the transition from the Ppy segment to Au. The illustration of the hydrated two-part rod shows the measured difference in radius of the Au and Ppy segments (Δr) and its standard deviation as measured for six rods. Statistical data can be found in the Supporting Information.

μm. This distance remains constant for rods within the template (red line, Figure 3a) and when the template has been dissolved (Figure 3b). When the bulk water has receded from the structure, contraction can be clearly observed (Figure 3c). The amount of contraction (83.2 ± 4.1%)[7] is slightly more than ideal contraction (92%), but is reasonable when one considers void spaces (missing rods) and three-dimensional reorganization. Capillary assembly of AAO-based nanorods has been independently confirmed by McCarley *via* the use of freeze-drying and Frank *via* the use of $scCO_2$ which eliminate capillary forces.[28,29]

The long-range nature of the capillary forces has two important implications for the assembly process. One, it provides defect tolerance. For example, in instances where the pattern of rods is mishandled and broken into multiple segments, capillary forces are strong enough to draw the sections back into contact with the main structure (Figure 3d,e). Flaws spanning distances of up to 40 μm have been "healed" in this manner. Two, patterns in the same droplet of water can be easily drawn together and would be expected to adhere to each other. While attraction and contact occur randomly, we have found one clear instance (in over 500 structures) where capillary forces have drawn two structures together such that they remain in adhesive contact (Supporting Information, Figure S2). This is minimized in our procedure by diluting the water which contains the structures and ensuring only one structure is contained per droplet, which is then allowed to dry.

Adhesive Forces and Polymer Dehydration. After the water has evaporated and assembled the nanorods into a close packed form, adhesive forces dominate.[30] These forces are expected to maintain the contact between the Ppy sections even as the polymer dehydrates and shrinks[7,31] to give the final curved superstructure. The modeling of the adherence force requires calculation of the adhesive force which compresses both segments (resulting in deformation) and a restorative (Hertzian) force opposite in direction to the adhesive force (Figure 4a).[32]

The attractive forces for the two segments can be calculated independently only if the two sections are able to reach equilibrium compression without the influence of the other material. Surprisingly, this condition is met. Initially the polypyrrole section is slightly swollen and adhesion between these sections dominates. Tapping mode atomic force microscopy, performed in aqueous environment identical to assembly conditions, shows a small but significant amount of swelling of the polymer section of the nanorod. As measured at the interface of the gold and polymer, the radius difference is 11.5 ± 9.7 nm (Figure 4b and Supporting Information, Figure S3). As this segment shrinks during polymer dehydration, the Au segments are brought closer together until they have reached equilibrium, and the contact zone is maximized. Once both segments have reached equilibrium the Ppy continues to shrink and the segments pull on each other until the pull-off force of the Au segment is exceeded, contact is broken, and the rods splay.

Deformation and adhesion can be modeled by Johnson−Kendall−Roberts (JKR), Derjaguin−Muller−Toporov (DMT), or Maugis−Dugdale (MD) theory, with a transition parameter λ_{trans}[33] determining the applicability of approximations contained in each theory.[34] In deriving a cohesive zone model[35] for the cylindrical geometry, Hui showed that JKR theory was applicable for a λ_{trans} of 4 or greater; for $\lambda_{trans} < 4$ cohesive zone models are of higher accuracy.[36] We find that for both Au and Ppy, the JKR theory is applicable (Supporting Information).

According to JKR theory, the restoration forces from deformation (per unit length) are equal to $\pi h^2 E^*/(4R)$ and the adhesion forces are $-(2\pi E^* hW)^{1/2}$ (h is the half contact length, Figure 4a; W, R, and E^* are defined in Table 1).[37,38] Using these expressions, we find that for perfectly smooth cylinders the pull-off force P_{max} (the maximum force necessary to separate the two rods)

TABLE 1. Materials Properties of Ppy and Au Used in the Calculation of the Forces and Energies between Two Rods

Mat'll	Young's modulus (E_i) [GPa]	Poisson's ratio (υ_i)	combined modulus ($E^* = [(1-\upsilon_1^2)/E_1 + (1-\upsilon_2^2)/E_2]^{-1}$) [GPa]	surface energy (γ) [J/m^2]	work of adhesion ($W = 2\gamma$) [J/m^2]	effective radius ($R = 1/(1/r_1 + 1/r_2)$) [nm]	$(W^2RE^*)^{1/3}$ [N/m]	$(W^4R^2/E^*)^{1/3}$ [J/m]	$(W_{eff}{}^4R^2/E^*)^{1/3}$ experimental ratio
Ppy	0.6[15,49]	0.4[15]	0.36	0.33[15]	0.66	98.3[7]	2.5	1.7×10^{-8}	7
Au	80[50,51]	0.42[51]	49	1.54[16]	3.07	92.5[7]	35	2.5×10^{-8}	1

scales as $(W^2RE^*)^{1/3}$ which is much larger for Au than for Ppy if the parameters from Table 1 are used. This calculation is in apparent conflict with the experiments showing that the stronger interactions between the Ppy segments result in the observed curved structures (Figure 1c,d). Two factors have been ignored in this explanation, which are important in our system and account for this apparent discrepancy. The first is that the net interaction energy between Au segments or Ppy segments is a more relevant quantity than the pulloff forces which make assumptions about the way the forces are applied. This energy scales roughly as $P_{max}{}^2/E^*$, by analogy to the relationship between the critical stress intensity factor and critical strain energy release rate in fracture mechanics.[39] This gives an interaction energy that scales as $(W^4R^2/E^*)^{1/3}$. Thus, due to the fact that Ppy's lower elastic modulus allows for greater compression and contact area, the net interaction energy between the Ppy segments is comparable to that between Au segments, as seen in Table 1.

The second factor that must be accounted for is the fact that the surfaces of the nanorods are not perfectly smooth, so that the actual contact area between the nanorods is less than the ideal value. The effect of roughness can be accounted for by replacing the actual value of W obtained from surface energies with an effective value that is substantially diminished.[40,41] An estimate of the relative decrease in the value of W for the two materials can be obtained by varying the segment lengths. As can be seen in Figure 5, when the ratio of the two segments is increased, the Ppy−Ppy interactions dominate until the Au:Ppy ratio is approximately equal to 7:1. At this point the Au−Au interactions dominate, and the superstructure no longer curves (Figure 5, bottom right image). Our qualitative explanation is that the roughness decreases W_{eff}, the effective value of the adhesion energy, so that $(W_{eff}{}^4R^2/E^*)^{1/3}$ is seven times larger for Ppy than it is for Au.

The mechanism of curving raises several interesting points. The most apparent is that the curving processes are dominated by the materials properties. Polypyrrole is unusual in that it has a relatively high surface energy for an organic polymer, yet it has a very low elastic modulus, which results in a highly attractive net interaction energy and curved superstructures at nearly any length. For example, if polystyrene or polypropylene were used, the force (and net interaction energy) per unit length would be smaller. If one uses values for the surface energy (~0.03 J/m^2) and elastic modulus (3 GPa) that are typical for most thermoplastics such as polystyrene and polypropylene, the interaction energies are less than that for Ppy by a factor of 40. The other segment (gold) has materials properties (elastic modulus and surface energy)[14,42] that are similar to many other metals and inorganic materials. Another interesting implication arises from the fact that polymer dehydration is essential to the curving. As our observations and calculations show, curving occurs as a result of adhesion/dehydration, a distinct step from capillary force assembly.

CONCLUSIONS

In summary, we have studied the mechanism by which hundreds of thousands of two-part gold−polypyrrole nanorods are assembled into discrete superstructures, dictated in large part by the choice of template. Four contributing factors were studied: the type of template, capillary forces, adhesion, and polymer dehydration. This work suggests that the combination of templating and capillary forces is virtually scale-independent, and is effective for a rod spacing of 200 nm or less (limited by templating) and a pattern spacing of similar dimension. The combination of adhesion and polymer dehydration dominates the structure

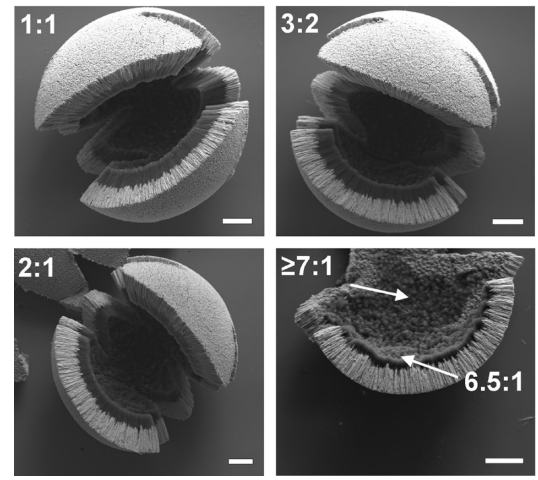

Figure 5. Superstructures generated from a sphere pattern, which have not closed completely. Here the Au:Ppy segment length ratios are clearly observable in the SEM images. As the Ppy segment length decreases, there is no discernible change in the superstructure curvature until the ratio of Au to Ppy exceeds 7:1, at which point the interaction energy between Ppy segments is less than that between Au segments. Curvature loss can be seen in the region labeled ≥7:1. A sampling of structures were fractured to confirm that the dimensions of the visible rods at the edge of the superstructure were representative of the bulk. The scale bars are 40 μm.

and provides the driving force for curvature until the Au:Ppy length ratio exceeds ~7:1, taking advantage of Ppy's unusually strong interactions. The versatility of this system, along with the rapid advancement of template generated nano-objects and patterns,[43−48] suggests that it is possible to deliberately make a wide variety of structures containing greater complexity in both shape and composition.

MATERIALS AND METHODS

Materials. Metal plating solutions were purchased from Technic. The gold solution (Orotemp 24 RTU) was purchased with a metal concentration of 0.25 troy oz/qt and the silver (1025 RTU) with 4.5 troy oz/gal. Ppy was polymerized from a homemade solution (340 μL of Ppy, 0.212 g of $LiClO_4$, 20 mL of H_2O).

Superstructure Preparation. Nanorods were electrochemically grown within the pores of Whatman 0.1 μm Anodisc membranes (pore working diameter was ≈ 0.37 μm, membrane diameter was 1.3 cm). The templates were prepared for the electrochemical steps by first thermally evaporating a silver layer (>150 nm) which serves as the working electrode, then adhering the silver backing to a silver coated microscope slide (>150 nm Ag). The silver slide provides electrical contact as well as a rigid substrate for the lithography steps. Polyethylene glycol acted as the adhesive.

Lithography was performed using commercial specifications and SU-8 (2025, Microchem) as a photoresist. The membrane was then subjected to electrochemical processes which deposited/polymerized the rod segments. A representative procedure for the 1:1 superstructures in Figure 5 follows. A sacrificial silver layer was deposited for 23 min (−900 mV *vs* Ag/AgCl, 0.38 C of charge), followed by gold (−900 mV *vs* Ag/AgCl, 200 min, 2.16 C) and Ppy (750 mV *vs* Ag/AgCl, 20 min, 0.82 C). Afterward, the template was exposed to CH_2Cl_2 (5 min) to remove the photoresist. This was followed by HNO_3 (5 min) to remove the silver and 3 M NaOH (5 h) to remove the alumina template. The structures, held together only by loose interactions, were rinsed with Nanopure H_2O (18.1 MΩ) and placed individually on a microscope slide where the water was allowed to evaporate. When the slide was coated with a low surface energy material (for example, octadecanethiol on gold) substrate−superstructure interactions were minimized and consistent structures were realized.

Acknowledgment. This work was supported by DARPA and the NSF Chemistry Division and by the MRSEC program of the NSF through the Northwestern University MRSEC. In addition, this work was supported by the Non-equilibrium Energy Research Center (NERC) which is an Energy Frontier Research Center funded by the U.S. Department of Energy, Office of Science, Office of Basic Energy Sciences under Award No. DE-SC0000989. J.W.C. thanks the American Cancer Society for a postdoctoral fellowship. C.A.M. is grateful for a NSSEF Fellowship. This work makes use of Central Facilities supported by the MRSEC and NSEC programs of the National Science Foundation at Northwestern University.

Supporting Information Available: Materials properties used in calculations, SEM images of AAO templates and superstructures, and AFM data used to determine rod diameters. This material is available free of charge *via* the Internet at http://pubs.acs.org.

REFERENCES AND NOTES

1. Clark, T. D.; Tien, J.; Duffy, D. C.; Paul, K. E.; Whitesides, G. M. Self-Assembly of 10-μm Sized Objects into Ordered Three-Dimensional Arrays. *J. Am. Chem. Soc.* **2001**, *123*, 7677–7682.
2. Kalsin, A. M.; Fialkowski, M.; Paszewski, M.; Smoukov, S. K.; Bishop, K. J. M.; Grzybowski, B. A. Electrostatic Self-Assembly of Binary Nanoparticle Crystals with a Diamond-like Lattice. *Science* **2006**, *312*, 420–424.
3. Tripp, S. L.; Dunin-Borkowski, R. E.; Wei, A. Flux Closure in Self-Assembled Cobalt Nanoparticle Rings. *Angew. Chem., Int. Ed.* **2003**, *42*, 5591–5593.
4. Park, S. Y.; Lytton-Jean, A. K. R.; Lee, B.; Weigand, S.; Schatz, G. C.; Mirkin, C. A. DNA-Programmable Nanoparticle Crystallization. *Nature* **2008**, *451*, 553–556.
5. Nykypanchuk, D.; Maye, M. M.; van der Lelie, D.; Gang, O. DNA-Guided Crystallization of Colloidal Nanoparticles. *Nature* **2008**, *451*, 549–552.
6. Kralchevsky, P. A.; Nagayama, K. Capillary Interactions between Particles Bound to Interfaces, Liquid Films, and Biomembranes. *Adv. Colloid Interface Sci.* **2000**, *85*, 145–192.
7. Ciszek, J. W.; Huang, L.; Wang, Y.; Mirkin, C. A. Kinetically Controlled, Shape-Directed Assembly of Nanorods. *Small* **2008**, *4*, 206–210.
8. Martin, C. R. Nanomaterials: A Membrane-Based Synthetic Approach. *Science* **1994**, *266*, 1961–1966.
9. Routkevitch, D.; Bigioni, T.; Moskovits, M.; Xu, J. M. Electrochemical Fabrication of CdS Nanowire Arrays in Porous Anodic Aluminum Oxide Templates. *J. Phys. Chem.* **1996**, *100*, 14037–14047.
10. Park, S.; Lim, J.-H.; Chung, S.-W.; Mirkin, C. A. Self-Assembly of Mesoscopic Metal-Polymer Amphiphiles. *Science* **2004**, *303*, 348–351.
11. Lim, J. K.; Ciszek, J. W.; Huo, F.; Jang, J.-W.; Hwang, S.; Mirkin, C. A. Actuation of Self-Assembled Two-Component Rodlike Nanostructures. *Nano Lett.* **2008**, *8*, 4441–4445.
12. Li, F.; Zhu, M.; Liu, C.; Zhou, W. L.; Wiley, J. B. Patterned Metal Nanowire Arrays from Photolithographically-Modified Templates. *J. Am. Chem. Soc.* **2006**, *128*, 13342–13343.
13. Tsonchev, S.; Schatz, G. C.; Ratner, M. A. Electrostatically-Directed Self-Assembly of Cylindrical Peptide Amphiphile Nanostructures. *J. Phys. Chem. B* **2004**, *108*, 8817–8822.
14. Israelachvili, J. *Intermolecular and Surface Forces*; Academic Press: New York, 1991.
15. Cuenot, S.; Fretigny, C.; Demoustier-Champagne, S.; Nysten, B. Surface Tension Effect on the Mechanical Properties of Nanomaterials Measured by Atomic Force Microscopy. *Phys. Rev. B* **2004**, *69*, 165410.
16. Tyson, W. R.; Miller, W. A. Surface Free Energies of Solid Metals: Estimation from Liquid Surface Tension Measurements. *Surf. Sci.* **1977**, *62*, 267–276.
17. Hyldgaard, P.; Einstein, T. L. Surface-State-Mediated Three-Adsorbate Interaction. *Europhys. Lett.* **2002**, *59*, 265–271.
18. Troisi, A.; Wong, V.; Ratner, M. A. Self-Assembly on Multiple Length Scales: A Monte Carlo Algorithm with Data Augmentation. *J. Chem. Phys.* **2005**, *122*, 024102.
19. Meyer, E. E.; Rosenberg, K. J.; Israelachvili, J. Recent Progress in Understanding Hydrophobic Interactions. *Proc. Natl. Acad. Sci. U.S.A.* **2006**, *103*, 15739–15746.
20. Horvolgyi, Z.; Mate, M.; Zrinyi, M. On the Universal Growth of Two-Dimensional Aggregates of Hydrophobed Glass Beads Formed at the (Aqueous Solution of Electrolyte)−Air Interfaces. *Colloids Surf., A* **1994**, *84*, 207–216.
21. Denkov, N. D.; Velev, O. D.; Kralchevsky, P. A.; Ivanov, I. B.; Yoshimura, H.; Nagayama, K. Mechanism of Formation of Two-Dimensional Crystals from Latex Particles on Substrates. *Langmuir* **1992**, *8*, 3183–3190.
22. Murray, C. B.; Kagan, C. R.; Bawendi, M. G. Self-Organization of CdSe Nanocrystallites into Three-Dimensional Quantum Dot Superlattices. *Science* **1995**, *270*, 1335–1338.
23. Ozin, G. A.; Yang, S. M. The Race for the Photonic Chip: Colloidal Crystal Assembly in Silicon Wafers. *Adv. Funct. Mater.* **2001**, *11*, 95–104.

24. Murray, C. B.; Kagan, C. R.; Bawendi, M. G. Synthesis and Characterization of Monodisperse Nanocrystals and Close-Packed Nanocrystal Assemblies. *Annu. Rev. Mater. Sci.* **2000**, *30*, 545–610.
25. Velev, O. D.; Denkov, N. D.; Paunov, V. N.; Kralchevsky, P. A.; Nagayama, K. Direct Measurement of Lateral Capillary Forces. *Langmuir* **1993**, *9*, 3702–3709.
26. Kralchevsky, P. A.; Denkov, N. D. Capillary Forces and Structuring in Layers of Colloid Particles. *Curr. Opin. Colloid Interface Sci.* **2001**, *6*, 383–401.
27. Kralchevsky, P. A.; Nagayama, K. *Particles at Fluid Interfaces and Membranes;* Elsevier: New York, 2001.
28. Chen, G.; Soper, S. A.; McCarley, R. L. Free-Standing, Erect Ultrahigh-Aspect-Ratio Polymer Nanopillar and Nanotube Ensembles. *Langmuir* **2007**, *23*, 11777–11781.
29. Zhu, K.; Vinzant, T. B.; Neale, N. R.; Frank, A. J. Removing Structural Disorder from Oriented TiO_2 Nanotube Arrays: Reducing the Dimensionality of Transport and Recombination in Dye-Sensitized Solar Cells. *Nano Lett.* **2007**, *7*, 3739–3746.
30. Kendall, K. Adhesion: Molecules and Mechanics. *Science* **1994**, *263*, 1720–1725.
31. Okuzaki, H.; Kunugi, T. Adsorption-Induced Bending of Polypyrrole Films and Its Application to a Chemomechanical Rotor. *J. Polym. Sci., Part B: Polym. Phys.* **1996**, *34*, 1747–1749.
32. Johnson, K. L. *Contact Mechanics*; Cambridge University Press: New York, 1985.
33. The use of lambda for both decay lengths ($\lambda_{Au,\ Ppy}$) and the transition parameter (λ_{trans}) is an attempt to be consistent with the prevailing terminology in different subdisciplines. Also, the reported values for surface tensions and energies vary greatly and often conflict. In the case of the surface energy of Ppy, we have chosen to use the surface tension value. The reported Ppy composition and surface tension measurement approximate our system better than reported surface energy values.
34. Johnson, K. L.; Greenwood, J. A. An Adhesion Map for the Contact of Elastic Spheres. *J. Colloid Interface Sci.* **1997**, *192*, 326–333.
35. Barenblatt, G. I. The Mathematical Theory of Equilibrium Cracks in Brittle Fracture. *Adv. Appl. Mech.* **1962**, *7*, 55–129.
36. Baney, J. M.; Hui, C.-Y. A Cohesive Zone Model for the Adhesion of Cylinders. *J. Adhes. Sci. Technol.* **1997**, *11*, 393–406.
37. Barquins, M. Adherence and Rolling Kinetics of a Rigid Cylinder in Contact with a Natural Rubber Surface. *J. Adhes.* **1988**, *26*, 1–12.
38. Chaudhury, M. K.; Weaver, T.; Hui, C. Y.; Kramer, E. J. Adhesive Contact of Cylindrical Lens and a Flat Sheet. *J. Appl. Phys.* **1996**, *80*, 30–37.
39. Lawn, B. *Fracture of Brittle Solids,* 2nd ed.; Cambridge University Press: New York, 1993.
40. Fuller, K. N. G.; Tabor, D. The Effect of Surface Roughness on the Adhesion of Elastic Solids. *Proc. R. Soc. London, A* **1975**, *345*, 327–342.
41. Johnson, K. L. Mechanics of Adhesion. *Tribol. Int.* **1998**, *31*, 413–418.
42. Lide, D. R. *CRC Handbook of Chemistry and Physics*, 83rd ed.; CRC Press: New York, 2002.
43. Lee, W.; Ji, R.; Gosele, U.; Nielsch, K. Fast Fabrication of Long-Range Ordered Porous Alumina Membranes by Hard Anodization. *Nat. Mater.* **2006**, *5*, 741–747.
44. Lee, W.; Schwirn, K.; Steinhart, M.; Pippel, E.; Scholz, R.; Gosele, U. Structural Engineering of Nanoporous Anodic Aluminium Oxide by Pulse Anodization of Aluminium. *Nat. Nanotechnol.* **2008**, *3*, 234–239.
45. Zhao, S.; Chan, K.; Yelon, A.; Veres, T. Novel Structure of AAO Film Fabricated by Constant Current Anodization. *Adv. Mater.* **2007**, *19*, 3004–3007.
46. Hurst, S. J.; Payne, E. K.; Qin, L.; Mirkin, C. A. Multisegmented One-Dimensional Nanorods Prepared by Hard-Template Synthetic Methods. *Angew. Chem., Int. Ed.* **2006**, *45*, 2672–2692.
47. Qin, L.; Park, S.; Huang, L.; Mirkin, C. A. On-Wire Lithography. *Science* **2005**, *309*, 113–115.
48. Chen, X.; Li, S.; Xue, C.; Banholzer, M. J.; Schatz, G. C.; Mirkin, C. A. Plasmonic Focusing in Rod−Sheath Heteronanostructures. *ACS Nano* **2009**, *3*, 87–92.
49. Cuenot, S.; Fretigny, C.; Demoustier-Champagne, S.; Nysten, B. Measurement of Elastic Modulus of Nanotubes by Resonant Contact Atomic Force Microscopy. *J. Appl. Phys.* **2003**, *93*, 5650–5655.
50. Kim, W. J.; Carr, S. M.; Wybourne, M. N. Direct Contact Buckling of Electrochemically Grown Gold Nanowires. *Appl. Phys. Lett.* **2005**, *87*, 173112.
51. Budakian, R.; Putterman, S. J. Force Detection Using a Fiber-Optic Cantilever. *Appl. Phys. Lett.* **2002**, *81*, 2100–2102.